



# On the Relationship Between Dislocation Creep Strength and Microstructure of a Solid-Solution-Strengthened Ni-Base Superalloy

H.M. Tawancy

(Submitted October 25, 2018; in revised form January 21, 2019; published online March 28, 2019)

It is shown that the dislocation creep strength of a solid-solution-strengthened Ni-base superalloy is critically dependent upon the cooling rate from the annealing temperature. This behavior is correlated with the effect of cooling rate on the morphology of  $M_{23}C_6$ -type carbide which precipitates at grain boundaries during cooling. Experiment shows that the creep strength is enhanced by rapid cooling which results in discrete carbide particles with irregular shape following a zigzag path along the grain boundaries. However, the creep strength is degraded as the morphology is changed into lamellar type by a discontinuous grain boundary reaction which occurs during slower cooling rates. Due to the transition from the discrete particle into the lamellar morphology, plastic deformation becomes more localized alongside the grain boundaries which accelerates the creep rate leading to premature intergranular failure. On the other hand, it is also shown that the stacking fault energy of the alloy increases with temperature which can allow dislocations to rearrange themselves into subgrain structure with relative ease during steady-state creep.

**Keywords** carbide precipitates, dislocation creep, electron microscopy, grain boundaries, nickel-base superalloys

## 1. Introduction

Solid-solution-strengthened superalloys which can be fabricated into wrought products are widely used as structural materials for various components used in the petrochemical and power generation industries among others. In addition to being wrought alloys, they also have potentially useful combination of high-temperature mechanical strength and environmental resistance (Ref 1). In many high-temperature applications, creep strength plays a key role in limiting component life. For example, Fig. 1 illustrates the failure of a pyrolysis furnace tube made of an alloy based upon the (Fe-Ni-Cr)-system by longitudinal creep rupture running normal to the direction of the circumferential (hoop) tensile stress generated by the internal fluid pressure. Therefore, since the resistance to creep rupture is an important design criterion, there is always a need for high-temperature alloys with improved creep strength.

Among the wrought Ni-base superalloys, Haynes alloy 230 has been developed with improved combination of mechanical strength and environmental resistance achieved by selecting the Ni-Cr-W as the base system (Ref 2). Tungsten is chosen to provide the primary source of solid-solution strengthening due to its larger atomic size, slower diffusivity in Ni as well as its effectiveness in reducing the stacking fault energy of Ni as compared to other transition metals particularly Mo (Ref 3). An

additional source of strengthening is provided by carbide precipitates (Ref 4-8). On the other hand, the environmental resistance is achieved by a highly protective layer of  $Cr_2O_3$  maintained by the synergistic effect of Cr and minor but critical additions of La and Si.

Recently, alloy 230 is being considered for structural applications in the forthcoming generation IV nuclear reactors which are required to operate at higher temperatures to meet the growing need for electric power (Ref 9-12). In such applications, the material is subjected to prolonged exposure at high temperatures reaching 900 °C or higher in the presence of mechanical stresses (Ref 9, 10). Therefore, high-temperature creep strength becomes an important material requirement (Ref 11, 12). It is noted here that wrought alloys of commercial grade such as alloy 230 are complex multi-component systems which can exist in various states of thermodynamic equilibrium with different transition kinetics from one state to another. As a result, a given alloy composition can assume different microstructures and properties with marked functional dependence on heat treatment procedures. Therefore, the present investigation has been carried out to correlate the dislocation creep strength of alloy 230 with microstructures produced by different heat treatment procedures. Particular emphasis has been placed upon the effect of heat treatment on the precipitation behavior of carbides and the deformation behavior.

## 2. Experimental Procedure

Sheet sample of alloy 230 about 3 mm in thickness was used in the present investigation. Its chemical composition is shown in Table 1 as measured by inductively coupled plasma atomic emission spectroscopy. The carbon content was measured by combustion calorimetry. For comparative purposes, Table 1 also shows the nominal composition of the alloy.

H.M. Tawancy, Center for Engineering Research, Research Institute, King Fahd University of Petroleum and Minerals, KFUPM Box 1639, Dhahran 31261, Saudi Arabia. Contact e-mail: tawancy@kfupm.edu.sa.

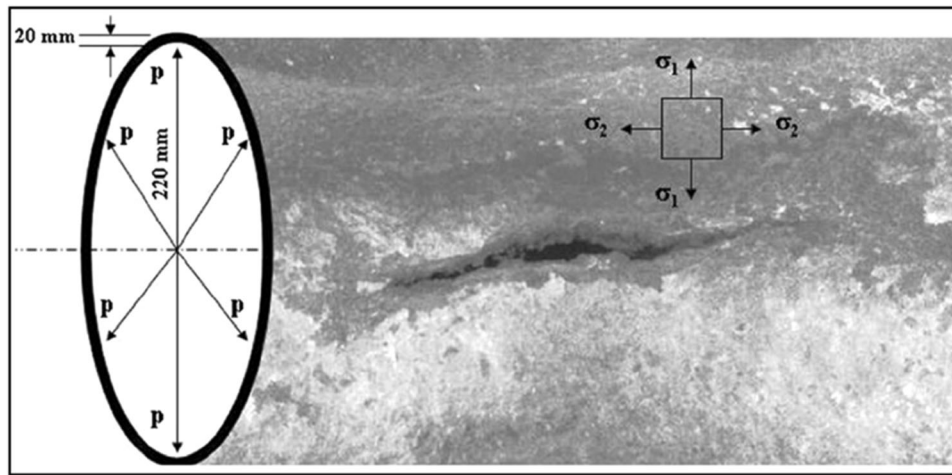


**Fig. 1** A macrograph illustrating longitudinal creep rupture of a pyrolysis furnace tube due to the circumferential (hoop) stress ( $\sigma_1$ ) produced by internal fluid pressure ( $P$ )

**Table 1** Chemical composition of alloy 230 (wt.%)

Element	Nominal	Measured
Ni	Balance	50.61
Cr	20-24	22.76
W	13-15	14.20
Mo	1-3	2.36
Co	4-6	4.10
Fe	2-4	3.65
Mn	0.3-1	0.72
Al	0.2-0.5	0.24
Ti	0.05-0.15	0.10
Si	0.25-0.75	0.63
La	0.005-0.05	0.02
Cu	0.4-0.6	0.44
C	0.05-0.15	0.13
B	0.01-0.02	0.01
S	0.01-0.02	0.01
P	0.02-0.04	0.02

Specimens for creep tests with 50.8 mm gage length were machined from the as-received sheet in addition to  $25.4 \times 25.4$  mm specimens for microstructural characterization. To determine the effect of cooling rate on the microstructure and creep strength, all specimens were divided into three sets. All sets were annealed for 20 min at 1200 °C as recommended by the manufacturer (Ref 13). To determine the effect of cooling rate on the microstructure and creep strength, one set was water quenched, another set was air-cooled and the third set was furnace-cooled. Also, some room-temperature tensile tests were carried out on specimens given the above heat treatment procedures as well as after aging for 4000 h at temperatures in the range of 500-1000 °C to characterize the thermal stability of the alloy.

The creep tests were carried out at 900 °C under constant load corresponding to a nominal stress of 40 MPa which is about 10% of the 0.2% room-temperature yield strength. During the tests, more than 100 strain/time data points were recorded by means of capacitive transducer and used to plot the creep curves. Some creep tests were interrupted at selected strains to characterize the respective deformation substructure.

However, except for the strain/time at failure, no data points were recorded for tests lasting more than 1000 h.

Specimens for optical microscopy were polished and then etched in a solution consisting of 80% HCl by volume and 20% chromic acid with concentration of 15 mol.%. Fractography was conducted in a scanning electron microscope (SEM) operating at 20 keV. Thin-foil specimens for transmission electron microscopy (TEM) were prepared by the jet polishing technique in a solution consisting of 30% nitric acid in methanol by volume. All the foils were examined at an accelerating voltage of 200 keV in an analytical electron microscope equipped with an energy-dispersive x-ray spectrometer and condenser lens system capable of focusing the electron beam down to 2 nm for both microchemical and microdiffraction analyses.

### 3. Experimental Results and Discussion

#### 3.1 Effect of Annealing Treatment on Microstructure and Tensile Strength

It is well known that the creep strength of a given alloy is critically dependent upon its thermal stability characteristics and tensile strength (Ref 14). On the other hand, the thermal stability is dependent upon the initial microstructure. Also, the primary creep stage is known to be history-dependent. It is then evident that a one-to-one correspondence exists between creep strength and the susceptibility to microstructural changes during exposure at elevated temperatures. Accordingly, it is expected that the creep strength of a given alloy is enhanced by an initial microstructure with higher thermal stability. Therefore, for a better understanding of the creep behavior, it is important to characterize the initial microstructure and its dependence on the heat treatment procedure as demonstrated in the present investigation.

Figure 2 shows an example illustrating the microstructure of alloy 230 produced by the heat treatment schedule recommended by the manufacturer (20 min at 1200 °C followed by water quenching (Ref 13)). The grain structure as observed on the scale of optical microscopy is shown in Fig. 2(a). Second-phase particles are observed both in the matrix and at grain

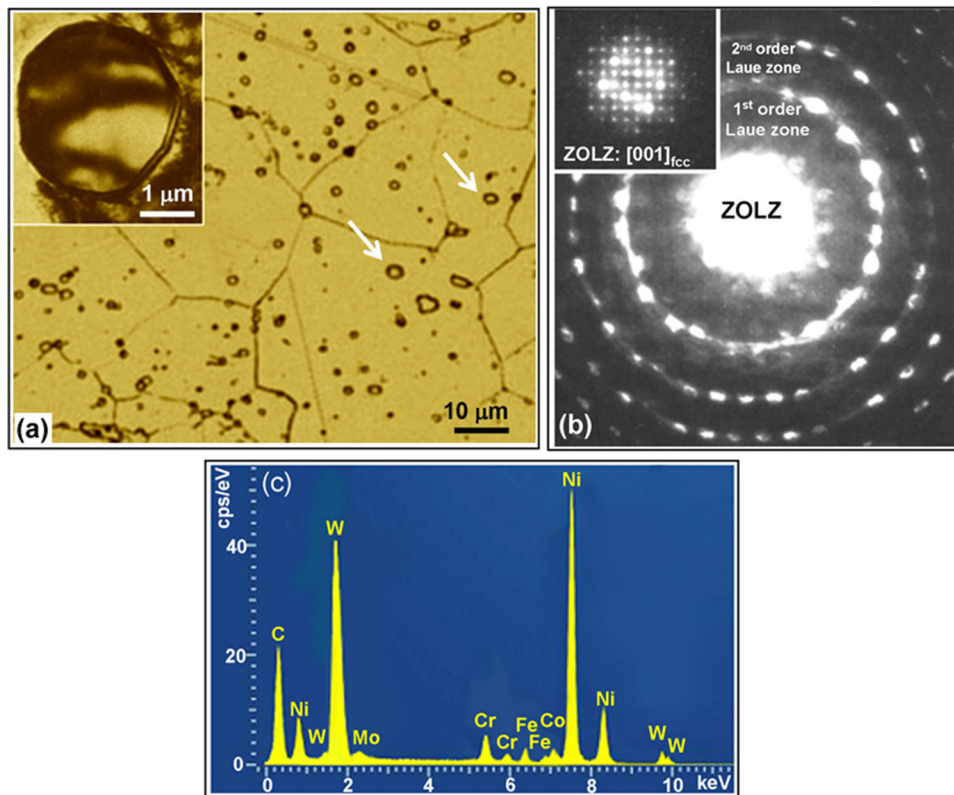


**Fig. 2** Identification of  $M_6C$ -type carbide in the annealed condition (1200 °C/20 min/water quenching). (a) Optical micrograph illustrating the gross grain structure; the arrows point at carbide particles and the inset is a bright-field TEM image showing a carbide particle. (b) Convergent-beam electron diffraction pattern in [001] cubic orientation derived from the particle in (a); the inset illustrates the zero-order Laue zone. (c) Energy-dispersive x-ray spectrum illustrating the elemental composition of the particle in (a)

boundaries. The inset shows a bright-field TEM image of a second-phase particle such as those indicated by the arrow in the optical micrograph. Figure 2(b) shows corresponding convergent-beam electron diffraction (CBED) pattern derived from the particle in Fig. 2(a). The zero-order Laue zone (ZOLZ) in the inset is observed to consist of a square array of spots. Both the ZOLZ and the higher order zones in the CBED show that the particle has a cubic structure with lattice parameter of about 1.10 nm consistent with  $M_6C$ -type carbide as further confirmed by the energy-dispersive spectrum of Fig. 2(c) which shows its elemental composition. It is observed that Ni and W are the major elemental constituents with minor concentrations of Mo and Cr. It is noted here that decomposition of  $M_6C$  carbide during subsequent exposure at high temperatures provides a source of C leading to precipitation of the Cr-rich  $M_{23}C_6$ -type carbide (Ref 15). As discussed later, this can have important effect on creep strength.

Further analysis of the grain structure on the scale of TEM has revealed the presence of another phase with finer particle size at the grain boundaries as illustrated in the example of Fig. 3. A bright-field TEM image showing second-phase particles at a grain boundary is shown in Fig. 3(a). Figure 3(b) shows a corresponding microdiffraction pattern typical of the cubic  $M_{23}C_6$  carbide in [001] orientation where the characteristic carbide reflections are observed at all one-third positions of the fundamental face-centered cubic (fcc) reflections of the matrix phase (200, 020, 220, etc.). Typically, the Cr-rich  $M_{23}C_6$  carbide maintains coherency with the matrix phase with cube-to-cube orientation relationship while having three times the

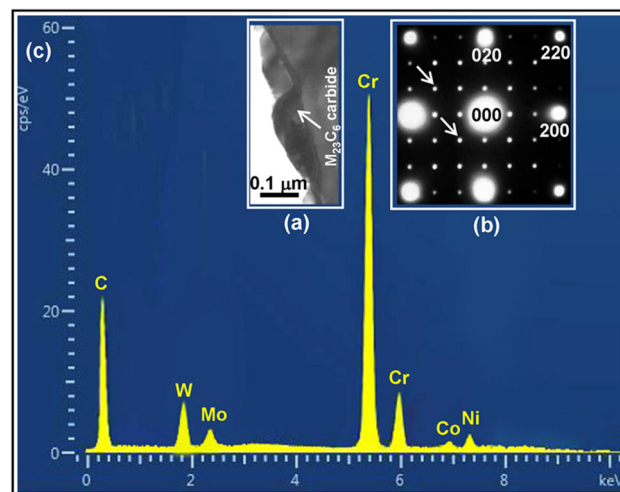


**Fig. 3** Identification of  $M_{23}C_6$ -type carbide at a grain boundary in the annealed condition (1200 °C/20 min/water quenching). (a) Bright-field TEM image illustrating the carbide particle morphology at a grain boundary. (b) Microdiffraction pattern derived from the particle in (a) in [001] cubic orientation; the characteristic carbide reflections at one-third positions of the matrix reflections (200, 020, 220, etc.) are indicated by the arrows. (c) Energy-dispersive x-ray spectrum illustrating the elemental composition of the particle in (a)

lattice parameter (1.08 nm) of the matrix (0.36 nm). As expected, the corresponding energy-dispersive spectrum of Fig. 3(c) shows that Cr is the major elemental constituent with



smaller concentrations of W and Mo. Although the  $M_{23}C_6$  carbide at the grain boundaries is observed to assume discrete particle morphology in the as-quenched condition (Fig. 3a), a significant change in morphology is observed to occur due to slower cooling rates from the annealing temperature as demonstrated below.

The effect of cooling rate on the room-temperature tensile strength is illustrated in the true stress–strain diagrams of

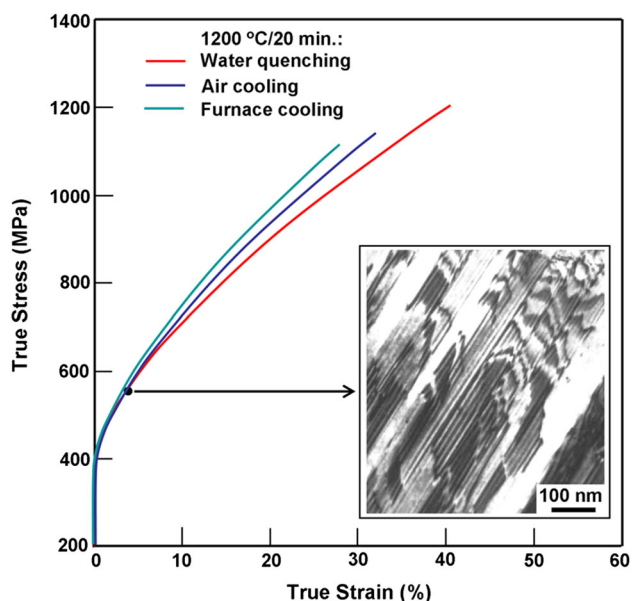


**Fig. 4** True stress–strain diagrams illustrating the effect of cooling rate from the annealing temperature (1200 °C/20 min) on the room-temperature tensile strength; the inset is a bright-field TEM image illustrating a typical deformation substructure corresponding to 4% strain

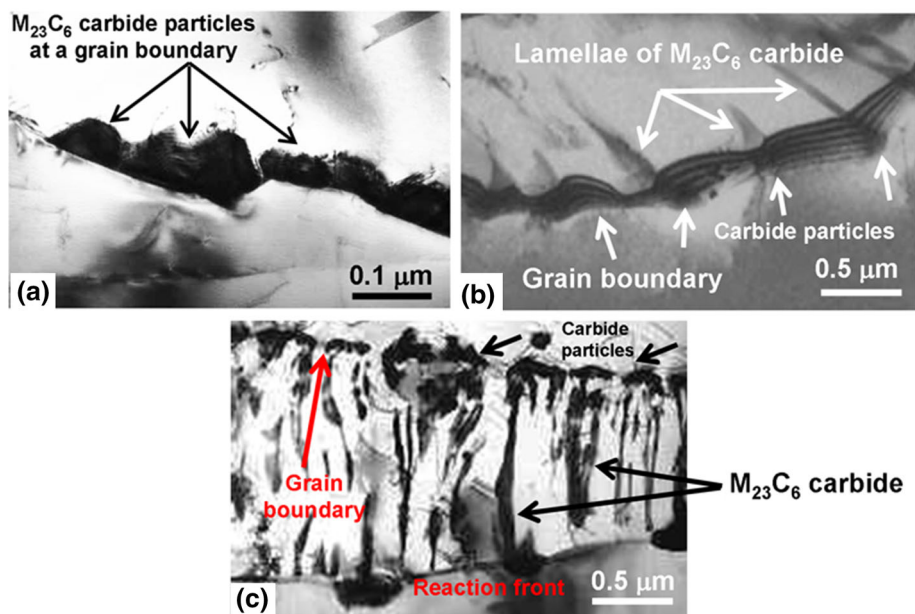
Fig. 4. Although the yield strength is not significantly affected, the tensile ductility is somewhat reduced with slower cooling rate. However, the cooling rate is found to have no effect on the deformation substructure which typifies a material with relatively low stacking fault energy as shown in the bright-field TEM image in the inset of Fig. 4 where high density of stacking faults with separated partial dislocations is observed (about 4% strain in the as-quenched specimen).

Figure 5 shows bright-field TEM images illustrating the effect of cooling rate on the morphology of  $M_{23}C_6$  carbide after 20 min of annealing at 1200 °C. As shown in Fig. 5(a), the carbide assumes discrete particle morphology with irregular shape in the as-quenched condition which usually follows a zigzag path along the grain boundaries. However, air cooling is found to promote a discontinuous precipitation reaction at the grain boundaries as shown in the example of Fig. 5(b). This results in a cellular structure consisting of alternating lamellae of carbide and alloy-depleted matrix. As illustrated in Fig. 5(c), the cell structure becomes well developed after furnace cooling. It is noted from Fig. 5(b) and (c) that the carbide lamellae emanate from small carbide particles at or very near the grain boundaries. This typifies type 2 reaction where the supersaturated matrix phase reacts with the preexisting coherent carbide particles to produce the lamellar structure which is known to be detrimental to mechanical strength (Ref 16).

As shown later, the microstructures shown in Fig. 5 are found to have significant effects on creep strength. Also, there is evidence that the stacking fault energy of the alloy increases with temperature, which facilitates the formation of dislocation cell structure during creep deformation.

### 3.2 Thermal Stability Characteristics

Figure 6 illustrates the effects of cooling rate from the annealing temperature of 1200 °C followed by 4000 h of aging at temperatures in the range of 500–1000 °C on the room-



**Fig. 5** Bright-field TEM images illustrating the effect of cooling rate from the annealing temperature (1200 °C/20 min) on the  $M_{23}C_6$  carbide morphology at the grain boundaries. (a) Water quenching (carbide particles are spread along a zigzag path along the grain boundary). (b) Air cooling (early stage of carbide precipitation by a discontinuous grain boundary reaction). (c) Furnace cooling (advanced stage of carbide precipitation by the discontinuous grain boundary reaction)

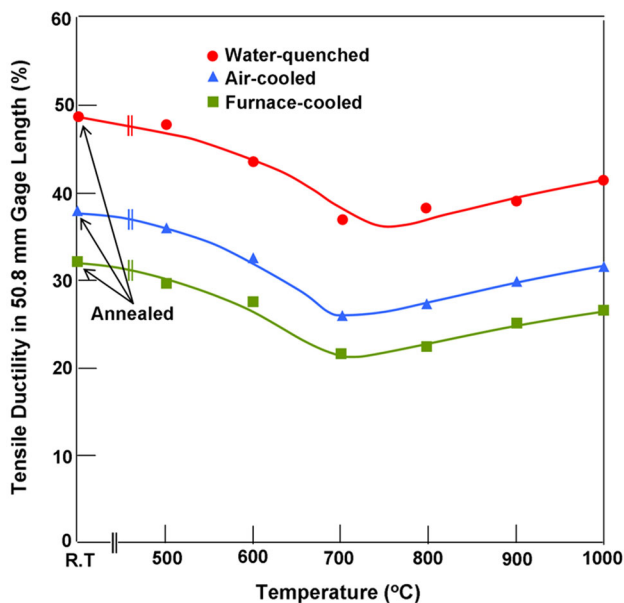


**Fig. 6** Effect of 4000 h of aging at temperatures in the range of 500-1000 °C on the room-temperature tensile ductility for various cooling rates from the annealing temperature (1200 °C/20 min)

temperature tensile ductility. It is observed that for each cooling rate, a tensile ductility minimum is observed at temperatures in the vicinity of 760 °C. However, the ductility is shifted to lower levels with slower cooling rate. Microstructural characterization has revealed that  $M_{23}C_6$  carbide is the only second phase precipitated in alloy 230 after the above aging conditions. Therefore, the observed loss in tensile ductility relative to the annealed condition for a given cooling rate can be correlated with precipitation of  $M_{23}C_6$  carbide. On the other hand, the lower ductility associated with slower cooling rates can be explained in terms of the variations in the initial microstructures shown in Fig. 5. Examples illustrating the precipitation characteristics of  $M_{23}C_6$  carbide during thermal aging are given below.

In general,  $M_{23}C_6$  carbide has long been known to precipitate in austenitic-type alloys during thermal aging at three preferential sites: (1) grain boundaries, (2) incoherent sides of twin boundaries and (3) preexisting dislocations (Ref 17). This is demonstrated for alloy 230 in the example of Fig. 7 which shows the effect of 4000 h of aging at 900 °C on the microstructure of water-quenched specimens. In this case, the grain boundary precipitation is observed to occur by a discontinuous mechanism as shown in the bright-field TEM image of Fig. 7(a). The inset is a microdiffraction pattern in [111] cubic orientation derived from the encircled region where

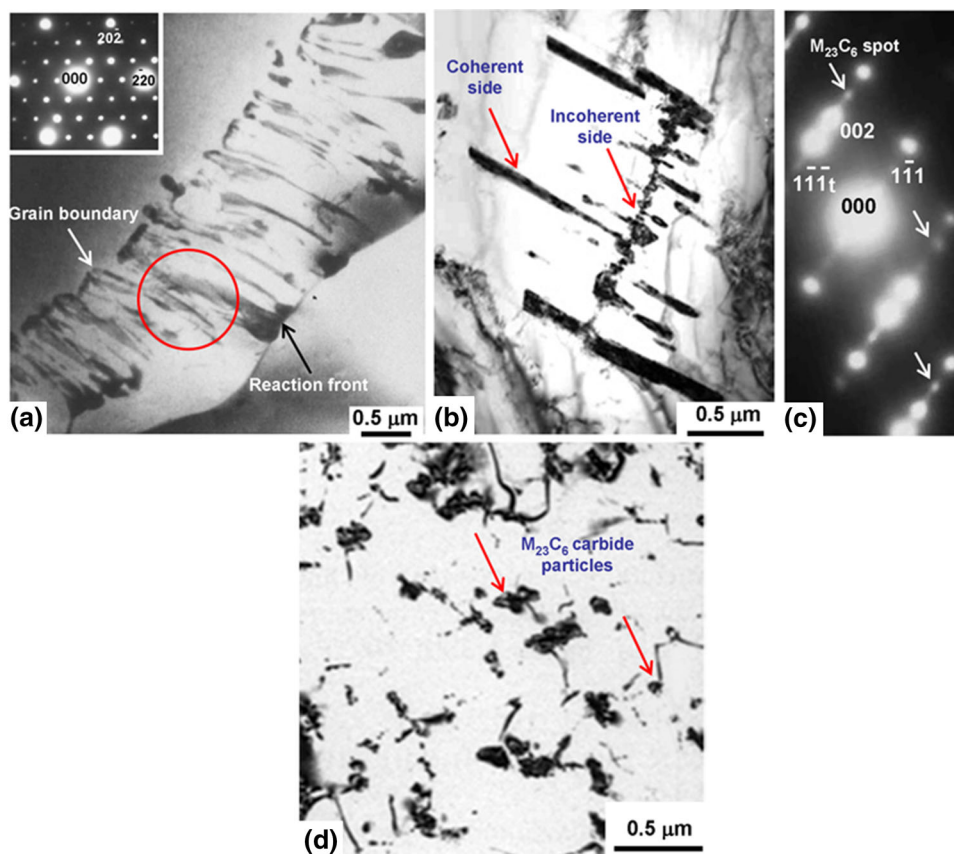


**Fig. 7** An example illustrating the precipitation sites of  $M_{23}C_6$  carbide after annealing (1200 °C/20 min/water quenching) + 4000 h of aging at 900 °C. (a) Bright-field TEM image illustrating the lamellar structure of  $M_{23}C_6$  carbide produced by the discontinuous reaction at a grain boundary; the inset is a microdiffraction pattern derived from the encircled region in [111] cubic orientation and showing the characteristic carbide reflections at all one-third positions of the fcc matrix reflections. (b) Bright-field TEM image showing carbide precipitates at twin boundaries. (c) Corresponding selected-area diffraction pattern in [110] cubic orientation showing characteristic twin and carbide reflections. (d) Bright-field TEM image illustrating  $M_{23}C_6$  carbide precipitate particles at preexisting dislocations

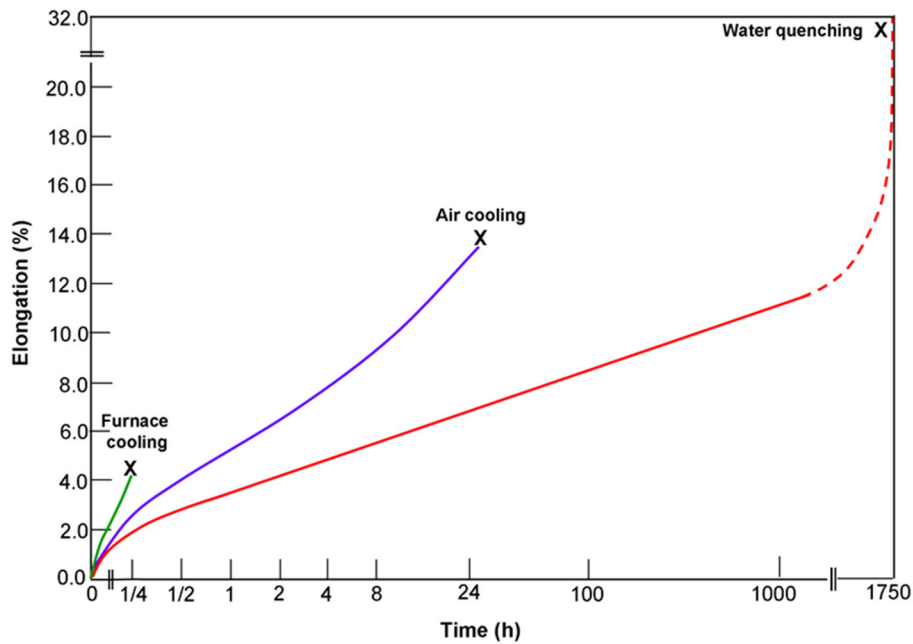


**Fig. 8** Effect of cooling rates on creep curves derived at 900 °C under a nominal stress of 40 MPa

the characteristic reflections of  $M_{23}C_6$  carbide are observed at all one-third positions of the matrix reflections. Precipitation at the twin boundaries is shown in the bright-field TEM image of Fig. 7(b) and the corresponding [110] cubic diffraction pattern of Fig. 7(c). Typically, the precipitation is initiated at the incoherent side of the boundary and growth occurs along the coherent side (Ref 18). The respective twin and  $M_{23}C_6$  carbide reflections are indicated in Fig. 7(c). Figure 7(d) is a bright-field TEM image showing  $M_{23}C_6$  carbide precipitates at preexisting dislocations. Since the creep tests were carried out at 900 °C, it is evident that the air- and furnace-cooled grain boundaries have been in more advanced stages of discontinuous grain boundary precipitation of  $M_{23}C_6$  prior to creep testing as compared to the as-quenched specimens. It is noted here that other than initial supersaturation in C, C released by decomposition of preexisting  $M_6C$  carbide can lead to precipitation of additional  $M_{23}C_6$  carbide during aging. Such precipitation is reflected on the creep strength as shown below.

### 3.3 Effect of Heat Treatment Procedure on Creep Strength

High-temperature creep deformation mechanisms of metals and alloys are commonly classified into: (1) dislocation creep which involves dislocation glide and climb, (2) grain boundary sliding and (3) diffusion flow caused by vacancies (Ref 14). Deformation due to dislocation creep solely occurs by motion, multiplication and rearrangement of dislocations at relatively low temperatures and high stress levels (Ref 19). In contrast, no dislocations are involved in the deformation caused by the other mechanisms, which become predominant at higher temperatures and lower stress levels (Ref 14).

It is well known that high-angle grain boundaries act as the major source of dislocations during the early stages of plastic deformation processes including dislocation creep (Ref 20). Precipitation of  $M_{23}C_6$  carbide at high-angle grain boundaries of Ni-base superalloys during either cooling from the annealing temperature or thermal aging is shown to be initiated by formation of irregularly shaped particles at concave positions of

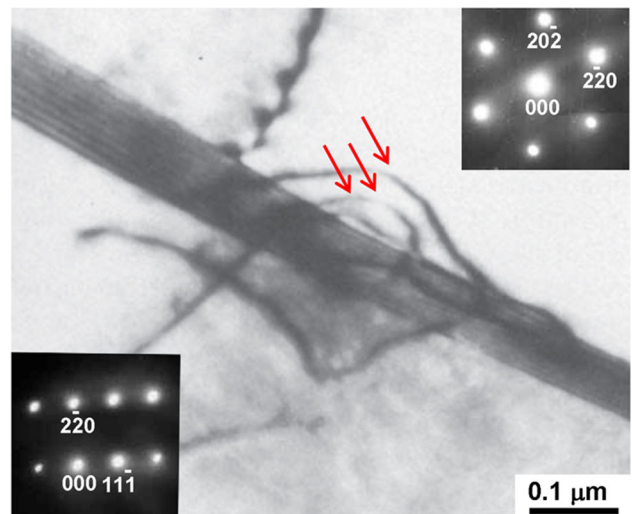


**Fig. 9** Bright-field TEM image illustrating a segment of a high-angle grain boundary free of carbide precipitate and acting as a dislocation source in a water-quenched specimen given about 1% creep strain during the primary stage (900 °C/40 MPa); the insets are selected-area diffraction patterns illustrating the [111] and [112] cubic orientations across the boundary, and the arrows point at some dislocations emanating from the boundary

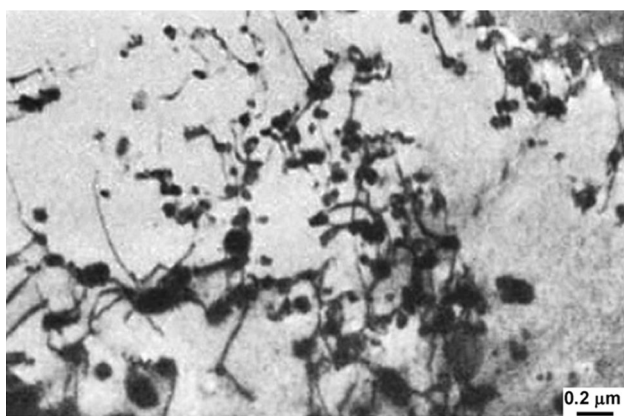
the boundary following a zigzag path (Ref 21) as shown in the example of Fig. 5(a). It is believed that this morphology reduces the ability of the boundary to act as an effective source of dislocations and therefore, it improves the creep strength (Ref 5, 21). However, development of the cellular grain boundary structures such as those shown in Fig. 5(c) and 7(a) can accelerate the creep rate as described below.

Figure 8 illustrates the functional dependence of the shape of creep curves generated at 900 °C under a nominal stress of 40 MPa on the cooling rate from the annealing temperature of 1200 °C. In the case of water quenching, a stage of primary



creep is followed by an extended stage of secondary creep. In contrast, an accelerated creep rate is observed in the case of furnace cooling indicating rapid transition from primary to tertiary creep reflecting the inability to strain harden during primary creep. Air cooling is shown to exhibit an intermediate behavior between water quenching and furnace cooling where primary creep is followed by a limited stage of secondary creep followed by tertiary creep. It is noted here that the effect produced by the transition from water quenching to furnace cooling is analogous to that of increasing the test temperature.

Figure 9 shows a bright-field TEM image of a carbide-free segment of high-angle grain boundary acting as a dislocation source during the early stage of primary creep (about 1% strain) in a water-quenched specimen. Dislocations emanating from the boundary are indicated by the arrows. The insets show the [111] and [112] cubic diffraction patterns illustrating the respective grain orientations across the boundary. Toward the end of the primary creep stage (about 3% strain), dislocation tangles are developed at  $M_{23}C_6$  carbide particles as illustrated



**Fig. 10** Bright-field TEM image illustrating tangles of dislocations at  $M_{23}C_6$  carbide particles in a water-quenched specimen given about 3% creep strain toward the end of the primary stage (900 °C/40 MPa)

in the bright-field TEM image of Fig. 10 which lead to strain hardening. Well-defined low-angle boundaries are observed during steady-state creep (about 7% strain) as shown in Fig. 11. A low-angle tilt boundary is shown in the weak-beam dark-field TEM image of Fig. 11(a). The insets show the respective two-beam conditions across each side of the boundary. A well-defined low-angle twist boundary is shown in the bright-field TEM image of Fig. 11(b). It is evident from these observations that the stacking fault energy of the alloy has increased with temperature allowing dislocations to move from one slip to another and rearrange themselves into low-angle boundaries. With continued creep deformation (about 10% strain), a cellular subgrain structure is developed as shown in the bright-field TEM images of Fig. 12. In this case, deformation is expected to be governed by dislocations crossing from one cell to another.

It is evident from the above observations that dislocation creep is the predominant deformation mechanism of alloy 230 at 900 °C/40 MPa, which is consistent with the measured creep strain exponents reported in Ref 22. Also, it is noted that earlier studies have shown that the stacking fault energy of many fcc metals and alloys increases with temperature (Ref 23). Since the respective stacking fault energy is roughly the difference between the energy of fcc and hexagonal close-packed structures (Ref 24), its increase with temperature is indicative of higher stability of fcc structures at higher temperatures.

### 3.4 Effect of Cooling Rate on the Fracture Mechanism

As an example, Fig. 13 shows secondary electron SEM images illustrating the effect of cooling rate from the annealing temperature on the morphology of surfaces exposed by fracture of creep-tested specimens. The furnace-cooled specimen (Fig. 13a) with an initial cellular carbide structure at the grain boundaries has fractured after about 15 min at 900 °C/40 MPa with 4% tensile elongation. It is observed that crack propagation has predominantly occurred along the grain boundaries. Also, secondary grain boundary cracks are observed. However, observation of the separated grain facts at high magnification has revealed morphological features characteristic of dimple-type rupture which occurs by microvoid coalescence as illustrated in the inset of Fig. 13(a). Such morphology is

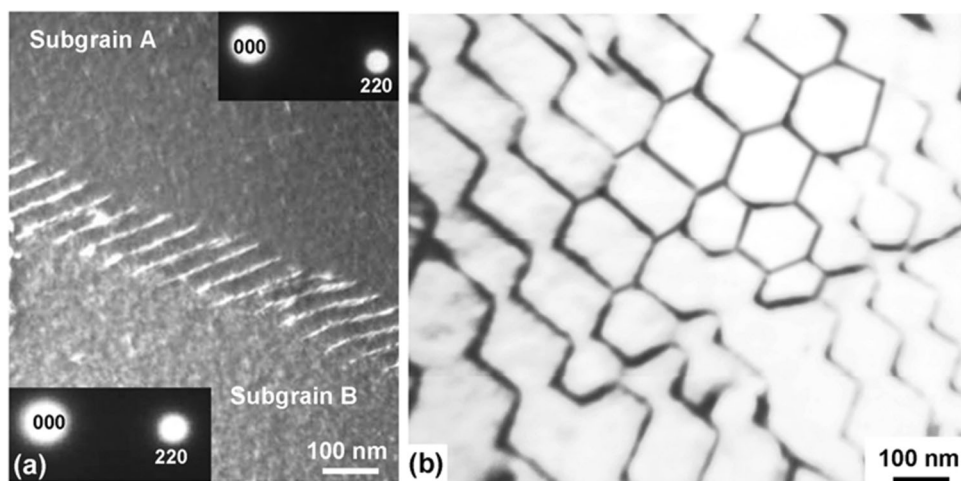


**Fig. 11** Observation of low-angle boundaries in a water-quenched specimen given about 7% creep strain during the steady state (900 °C/40 MPa). (a) Weak-beam dark-field image illustrating an array of dislocations at a low-angle tilt boundary; the insets show the two-beam diffraction conditions in subgrains A and B across the boundary. (b) Bright-field TEM image illustrating a hexagonal network of dislocations at a low-angle twist boundary

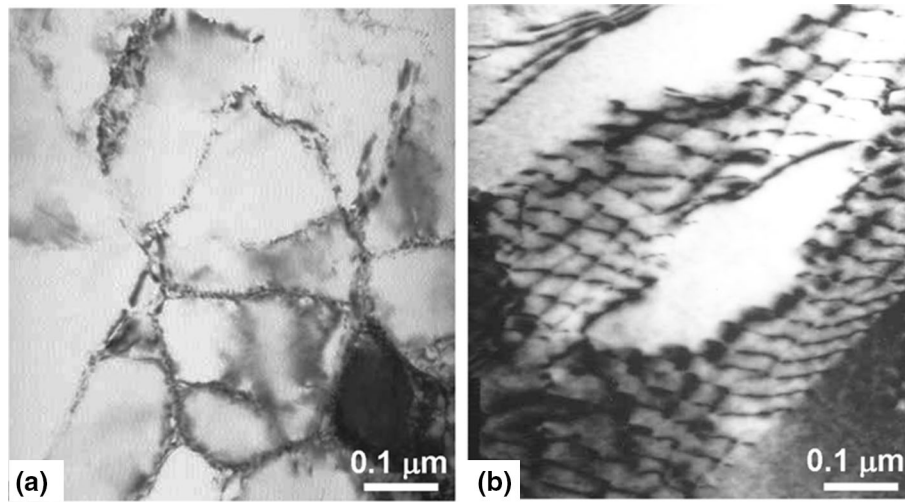


**Fig. 12** Observation of cellular subgrain structures in a water-quenched specimen given about 10% creep strain during the steady-state stage (900 °C/40 MPa). (a) Bright-field TEM image illustrating the cellular subgrain structure. (b) Bright-field image observed at a tilt angle allowing the observation of the dislocation structure at a cell boundary

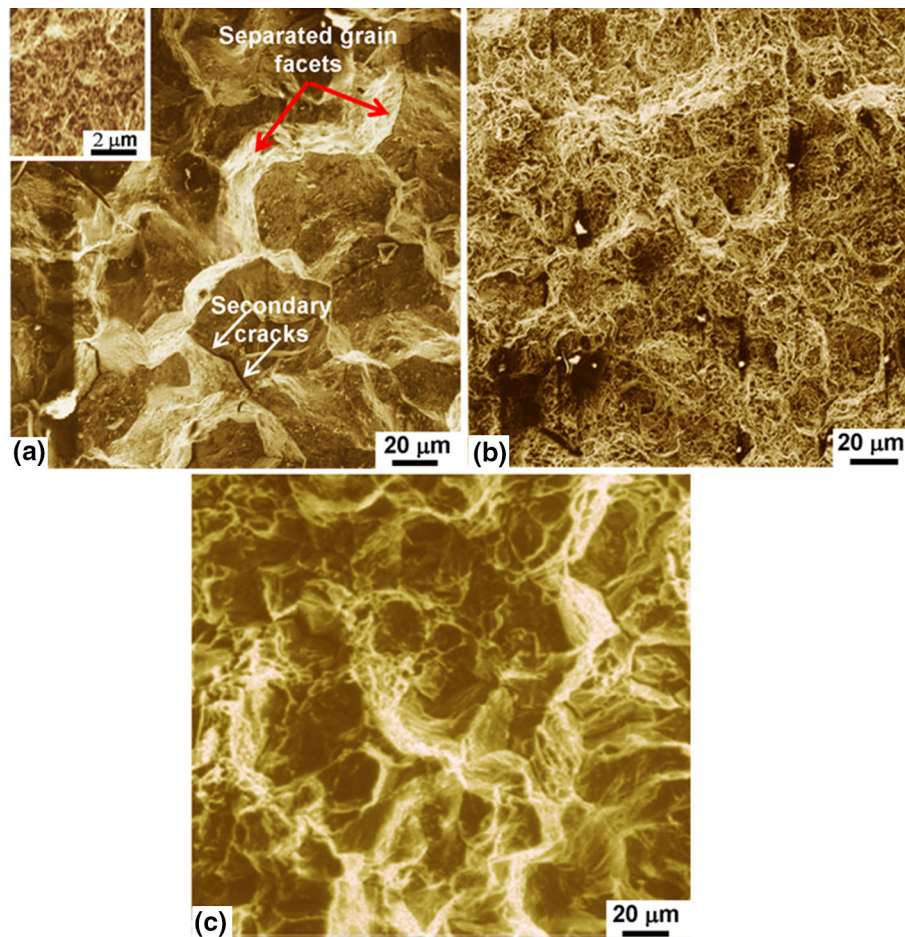


**Fig. 13** Secondary electron SEM images illustrating the effect of cooling rate from the annealing temperature (1200 °C/20 min) on the fracture mode of creep-tested specimens (900 °C/40 MPa). (a) Furnace-cooled: predominantly intergranular mode due to highly localized deformation alongside the grain boundaries; the inset is a high-magnification image showing the morphology of a separated grain facet. (b) Water-quenched: predominantly transgranular fracture mode. (c) Air-cooled: mixture of intergranular and transgranular

characteristic of ductile intergranular fracture mode which occurs due to localized plastic deformation in the softer alloy-depleted zones alongside grain boundaries. This behavior is

well known to be associated with the cellular grain boundary structures resulting from discontinuous precipitation reactions (Ref 16).



In contrast to the above behavior corresponding to furnace cooling, the water-quenched specimen has fractured after about 1750 h with 32% tensile elongation. Also, unlike the furnace-cooled specimen, fracture has predominantly occurred transgranularly by a ductile mechanism. The air-cooled specimen is found to exhibit somewhat intermediate behavior in that fracture has occurred after about 24 h with 13% tensile elongation. Also, Fig. 13(c) indicates that in addition to the intergranular mode, some of the fracture has also occurred transgranularly.

## 4. Conclusions

It is concluded from the present investigation that a one-to-one correspondence exists among initial microstructure, thermal stability and dislocation creep strength of alloy 230. This correspondence stems from the initial morphology of  $M_{23}C_6$  carbide precipitates at the grain boundaries and its functional dependence on the cooling rate from the annealing temperature. Discrete carbide particles produced by rapid cooling favor higher creep strength. However, with slower cooling rates, the carbide tends to precipitate by a discontinuous grain boundary reaction which degrades the creep strength. As a result, plastic deformation becomes more localized in the softer alloy-depleted zones alongside the grain boundaries which accelerates creep rate during the early stages of thermal exposure leading to premature intergranular failure. The results also demonstrate that the stacking fault energy of the alloy increases with temperature which allows dislocations to rearrange themselves into subgrain structure during creep deformation.

## Acknowledgments

The author is indebted for the continued support of King Fahd University of Petroleum and Minerals.

## References

1. L.M. Pike, 100+ Years of Wrought Alloy Development at Haynes International, in *8th International Symposium on Superalloy 710 and Derivatives*, ed. by E. Ott, A. Banik, X. Liu, I. Dempster, K. Heck, J. Anderson, J. Groh, T. Gabb, R. Helmink, A. Wusatowska-Sarneck (The Minerals, Metals and Materials Society, Warrendale, PA, 2014), p 15–30
2. H.M. Tawancy, D.L. Klarstrom, and M.F. Rothman, Development of a New Nickel-Base Superalloy, *J. Metals*, 1984, **36**, p 59–64
3. C.L. Zacherl, S.L. Shang, D.E. Kim, Y. Wang, and Z.K. Liu, Effect of Alloying Elements on Elastic, Stacking Fault Energy and Diffusion Properties of fcc Ni from First Principles: Implications for Tailoring the Creep Rate of Ni-Base Superalloys, *Superalloys 2012*, E.S. Huron, R.C. Reed, M.C. Hardy, M.J. Mils, R.E. Montero, P.D. Portella, and J. Teleman, Ed., The Minerals, Metals and Materials Society, Warrendale, PA, 2012, p 455–461
4. J.G. Yoon, H.W. Jeong, Y.S. Yoo, and H.U. Hong, Influence of Initial Microstructure on Creep Deformation Behavior and Fracture Characteristics of Haynes 230 Superalloy at 900 °C, *Mater. Charact.*, 2015, **101**, p 49–57
5. S. Chatterjee and A.K. Roy, Mechanism of Creep Deformation of Alloy 230 Based on Microstructural Analyses, *Mater. Sci. Eng. A*, 2010, **527**, p 7893–7900
6. T. Zengwu, L. Jinshan, H. Rui, L. Yi, and B. Guanghai, Effects of Solution Heat Treatment on Carbide of Ni-Cr-W Superalloy, *Rare Metal Mater. Eng.*, 2010, **39**, p 1157–1161
7. J. Veverkova, A. Strang, G.R. Marchant, G.M. McColvin, and H.V. Atkinson, High Temperature Microstructural Degradation of Haynes Alloy 230, *Superalloys 2008*, R.C. Reed, K.A. Green, P. Caron, T.P. Gabb, M.G. Fahrman, E.S. Huron, and S.A. Woodard, Ed., The Minerals, Metals and Materials Society, Warrendale, PA, 2008, p 479–488
8. H.M. Tawancy, High Temperature Creep Behavior of Ni-Cr-W-B Alloy, *J. Mater. Sci.*, 1992, **27**, p 6481–6489
9. J.L. King, H. Jo, A. Shahsafi, K. Blomstrand, K. Sridharan, and M.A. Kats, Impact of Corrosion on the Emissivity of Advanced Reactor Structural Alloys, *J. Nucl. Mater.*, 2018, **58**, p 465–471
10. P. Hosemann and J. Vujic, Materials Issues for Current and Advanced Nuclear Reactor Design, *Contemp. Mater.*, 2014, **1**, p 12–25
11. W. Ren and R. Swindeman, A Review on Current Status of Alloys 617 and 230 for Generation IV Nuclear Reactor Internals and Heat Exchangers, *J. Press. Vessel Technol.*, 2009, **131**, p 044002.1–044002.15
12. T. Allen, J. Busby, M. Meyers, and D. Petti, Materials Challenges for Nuclear Systems, *Mater. Today*, 2010, **13**, p 14–23
13. Haynes 230 Alloy Brochure, Haynes International Company, Kokomo, Indiana Publication No. H-3000K, 2017. [www.haynesintl.com/pdf/h300k/pdf](http://www.haynesintl.com/pdf/h300k/pdf)
14. M.E. Kassner, *Fundamentals of Creep in Metals and Alloys*, 2nd ed., Elsevier, Amsterdam, 2009, p 3–29
15. E.W. Ross and C.T. Sims, Nickel-Base Alloys, *Superalloys II*, C.T. Sims, N.S. Stoloff, and W.C. Hagel, Ed., Wiley, New York, 1987, p 97–134
16. D.B. Williams and E.P. Butler, Grain Boundary Discontinuous Reactions, *Int. Metals Rev.*, 1981, **126**, p 153–184
17. M.H. Lewis and B. Hattersley, Precipitation of  $M_{23}C_6$  in Austenitic Steels, *Acta Metall.*, 1965, **13**, p 1159–11681
18. N. Terao and B. Sasmal, Precipitation of  $M_{23}C_6$  Type Carbide on Twin Boundaries in Austenitic Stainless Steels, *Metallography*, 1980, **13**, p 117–133
19. W. Blum and P. Eisenlohr, Dislocation Mechanics of Creep, *Mater. Sci. Eng. A*, 2009, **510**, p 7–13
20. R.A. Varin, K.J. Kurzydowski, and K. Tangri, Analytical Treatment of Grain Boundary Sources of Dislocations, *Mater. Sci. Eng.*, 1987, **85**, p 115–126
21. Y. Zhang and F.D.S. Marquis, Effect of Grain Boundary Morphology and Dislocation Substructure on the Creep Behavior of Udimet 710, *Superalloys 1996*, R.D. Kissinger, D.J. Deye, D.I. Anton, A.D. Cetel, M.V. Nathal, T.M. Pollock, and D. Woodford, Ed., The Minerals, Metals and Materials Society, Warrendale, PA, 1996, p 391–399
22. C.J. Boehlert and S.C. Longanbach, A Comparison of the Microstructure and Creep Behavior of Cold Rolled HAYNES 230 Alloy and HAYNES 282 Alloy, *Mater. Sci. Eng. A*, 2011, **528**, p 4888–4898
23. L. Remy and A. Pineau, Temperature Dependence of Stacking Fault Energy in Close-Packed Metals and Alloys, *Mater. Sci. Eng.*, 1978, **36**, p 47–63
24. P.R. Swann, Dislocation Arrangements in Face-Centered Cubic Metals and Alloys, *Electron Microscopy and Strength of Crystals*, G. Thomas and J. Washburn, Ed., Wiley, New York, 1963, p 131–181

**Publisher's Note** Springer Nature remains neutral with regard to jurisdictional claims in published maps and institutional affiliations.